Simulation of Persistent Aircraft Contrails for Assessment of Climate Impact

Alexander D. Naiman

Ph.D. Candidate

Department of Aeronautics and Astronautics

Stanford University

Research Advisors

Sanjiva K. Lele

Department of Aeronautics and Astronautics

Mark Z. Jacobson

Department of Civil and Environmental Engineering

Submitted to the 7th Annual Joseph A. Hartman Student Paper Competition

24 January 2011

Contents

Abstract

The development of persistent contrails was modeled to determine the sensitivity of their climate-relevant properties to various parameters. Optical depth and area coverage varied most strongly with vertical shear. For a 4-engine aircraft and 130% ambient relative humidity with respect to ice, a moderate shear of $0.005\,\mathrm{s}^{-1}$ reduced the peak depth by 79% and increased the coverage by 450% after twenty minutes compared to a zero shear case. Depth was also sensitive to aircraft type and humidity, but variations in coverage were small. In these cases, larger aircraft and higher humidity resulted in larger depths.

1 Introduction

Commercial aviation impacts climate by two main avenues: the emission of greenhouse gases and cloud effects. While the former impact is similar to other activities that contribute to anthropogenic climate change, the latter is unique to aviation. As the growth of aviation continues to outstrip other industries (e.g., Lee et al. (2009), Fig. 3), understanding its impact on the environment becomes more vital.

In quantitative terms, a recent study gives the estimate of total aviation radiative forcing as 78 (38 to 139) mWm^{-2} for 2005, where these values refer to the best (low to high) estimates with a 90% likelihood range (Lee et al., 2009). The contribution of linear contrails to this total is 11.8 (5.4 to 25.6) mWm^{-2}, while aviation-induced cloudiness (AIC) accounts for 33 (12.5 to 86.7) mWm^{-2}. These two cloud effects introduce a large fraction of the overall uncertainty in the positive forcing due to aviation. The level of scientific understanding of contrail and induced cloudiness impacts were assessed as "low" and "very low" respectively in the same study.

Uncertainty in contrail radiative forcing arises from difficulty in estimating global coverage and optical properties of these anthropogenic clouds. Likewise, uncertainty in estimating AIC radiative forcing is due to the difficulty of observing and modeling the processes by which aviation induces cloudiness (Lee et al., 2009). This report seeks to reduce uncertainties and improve estimates of climate impacts by examining data produced by high fidelity simulations of contrail development. In the simulations, contrail fluid dynamic and microphysical processes are modeled under a variety of conditions. The properties of contrails under these conditions are assessed, and the data can then be used to improve global models used to estimate climate impacts.

This section gives a description of how contrails develop, an overview of previous work in contrail modeling, and a summary of the approach taken in this study. Section 2 describes the contrail model methodology and the cases simulated. Section 3 presents the results of the simulations and discusses the data. Finally, Section 4 reviews conclusions drawn from the data and suggests directions for future work.

1.1 Contrail Development

A brief overview of contrail development is helpful for discussing the approaches taken in contrail modeling. Contrails form when jet exhaust, laden with water vapor, volatile particles, and soot from fossil fuel combustion, interacts with the cold ambient atmosphere. Under certain conditions, water vapor condenses and freezes on condensation nuclei (e.g., emitted soot particles). These ice particles may evaporate or sublimate

quickly if the ambient air is dry, but when the air is supersaturated with respect to ice, they persist and grow (Schumann, 2005). These persistent contrails are the focus of this work.

From a dynamical standpoint, the development of contrails can be split into three distinct regimes: the jet, vortex, and dispersion phases. In the jet phase, contrail ice particles form in the exhaust and their motion is dominated by the jet. After a few seconds, the jet velocity subsides, and the vortex wake created by the lifting wing entrains the exhaust and particles. During this vortex phase, the vortices descend and carry the majority of the contrail with them. Some exhaust and contrail particles detrain from this primary wake due to buoyancy, forming a vertical curtain, also called the secondary wake. As the primary wake descends, vortex interactions eventually cause the vortex system to collapse and dissipate (Crow, 1970).

Once the organization of the vortex system has collapsed, the contrail enters the dispersion phase. At first, the contrail is dispersed by energy remaining from the vortex system. Vertical oscillations occur due to remaining buoyancy of the hot jet exhaust and descent of the vortex system in the presence of stable stratification. As these motions damp out, the contrail continues to spread due to atmospheric turbulence. Other effects such as radiative heating/cooling and sedimentation of large ice particles may further disperse the contrail.

1.2 Previous Work

Much of the previous modeling of contrails has been by large eddy simulation (LES), and this is the approach of the present study. Jensen et al. (1998) focused on the effect of radiative heating in their two-dimensional LES of the late dispersion phase. Three-dimensional LES by Chlond (1998) investigated a range of ambient temperature, humidity, and stability conditions, again in the late dispersion phase. Lewellen and Lewellen (2001) used a three-dimensional LES and studied both the vortex phase and the early dispersion phase for a range of conditions and aircraft types. Paoli et al. (2003) and Paoli et al. (2004) also studied the jet phase and early vortex phase with three-dimensional LES.

More recently, Unterstrasser et al. (2008) developed a two-dimensional model of the vortex phase that uses a parameterization to account for the dissipation of the vortex system, which is a fundamentally three-dimensional effect. The results of this study were then used to initialize fields for further two-dimensional simulations of contrails from the end of the vortex phase to several hours into the dispersion phase (Unterstrasser and Gierens, 2010a,b). Parametric variations in these studies included ambient humidity, temperature, vertical wind shear, and stratification, emitted ice crystal number, radiative effects, secondary nucleation effects, and supersaturated layer depth. Another recent study took a similar two-phase approach,

conducting three-dimensional LES first of the vortex and early dispersion phase, then of the late dispersion phase (Paugam et al., 2010). The focus was on the interaction between vortex dynamics and ambient turbulence with a single aircraft type and atmospheric condition.

1.3 Present Study Approach

This work simulates the development of contrails from the beginning of the vortex phase through the early dispersion phase, twenty minutes after emission. A three-dimensional large eddy simulation is used to resolve the energy-carrying scales of the flow. Ice particles are modeled using a Lagrangian tracking scheme and are coupled to the Eulerian fluid simulation through scalar source terms. The fluid phase solver uses an unstructured grid, which helps balance computational cost with resolution concerns and achieve a higher spatial resolution than previous studies. The Lagrangian ice tracking scheme also allows balancing of cost and resolution in representing spatial and size distributions of ice particles as the contrail develops.

This study includes a parametric variation of conditions including ambient turbulence, vertical wind shear, aircraft type, and ambient humidity. In presenting the results, the focus is on the aspects of contrails most relevant to their climate impact. As noted above, much of the uncertainty in estimating this impact is due to a lack of data concerning contrail coverage and contrail optical properties. The data presented therefore shows the sensitivity of contrails with respect to their ice content and geometric extent under the parametric variations.

2 Methodology

2.1 Computational Methods

The LES model solves the incompressible Navier-Stokes equations with a Boussinesq approximation for buoyancy forces. The numerical scheme uses a finite volume spatial discretization and an implicit fractional-step method for time advancement, with second order accuracy in both space and time (Mahesh et al., 2004; Ham et al., 2007). The fluid phase equations are solved on an unstructured, Eulerian grid for the resolved scales and the unresolved scales are modeled using a dynamic Smagorinsky model. Contrail ice particles are modeled using a Lagrangian tracking approach and a microphysical model of growth due to ice deposition and sublimation, similar to Paoli et al. (2004).

The computational domain is stationary with respect to the ground, so the computation represents a temporal simulation. The coordinate axes are positioned such that the y-axis is vertical (opposite gravity),

the z-axis points in the flight direction, opposite the cruise velocity, and the x-axis is the cross-stream direction. In the following dimensional coupled fluid equations, $\mathbf{u} = u\mathbf{i} + v\mathbf{j} + w\mathbf{k}$ is the air velocity vector, $\mathbf{g}$ is the gravitational acceleration vector, ν is the kinematic viscosity of air, κ is the thermal diffusivity of air, and D_v is the diffusivity of water vapor in air. The variables p, ρ, θ, and Y represent air pressure, air density, potential temperature, and water vapor density respectively. These are decomposed in the form $f(x, y, z, t) = f_0 + f_y(y) + f'(x, y, z, t)$, where f_0 is a constant reference part, f_y is an altitude varying part, and f' is a perturbation part. The variable ϕ represents a passive exhaust scalar with diffusivity D_v.

$$\nabla \cdot \mathbf{u} = 0 \tag{1}$$

$$\frac{D\mathbf{u}}{Dt} = -\frac{1}{\rho_0}\nabla p' + \frac{\rho'}{\rho_0}\mathbf{g} + \nu\nabla^2\mathbf{u} \tag{2}$$

$$\frac{\rho'}{\rho_0} = \frac{-\theta'}{\theta_0} \tag{3}$$

$$\frac{D\theta'}{Dt} = -\frac{d\theta_y}{dy}v + \kappa\nabla^2\theta' + \omega_T \tag{4}$$

$$\frac{DY'}{Dt} = -\frac{dY_y}{dy}v + D_v\nabla^2 Y' + \omega_Y \tag{5}$$

$$\frac{D\phi}{Dt} = D_v\nabla^2\phi \tag{6}$$

Equations 1 and 2 describe the incompressible Navier-Stokes equations with a Boussinesq approximation for buoyancy forces. The Boussinesq approximation gives the equation of state, Eq. 3, relating perturbation density to perturbation temperature (Spiegel and Veronis, 1960). Two scalar equations are solved for temperature and water vapor density (Eq. 4 and 5). For these simulations, the altitude varying part of these variables is prescribed as a constant gradient and the transport equations are solved for the perturbation parts. These two equations also include source terms (ω_T and ω_Y) that couple the deposition/sublimation of ice to the temperature equation through latent heat release as described below. Equation 6 is solved for the transport of a purely passive scalar.

The contrail ice particle positions are tracked using a Lagrangian approach. Computational particles, each

representing N_p physical particles, are tracked throughout the simulation. Fluid velocities from the Eulerian grid are interpolated to each particle location, which is then advanced using a third-order Runge-Kutta time integration. In the cases presented here, particles are treated as tracers of the fluid, an approximation that is suitable when particle relaxation times are short compared to flow time scales. This approximation is well-justified at early stages of contrail development when Stokes numbers are small, on the order of 10^{-4}, as they are throughout these simulations. A validation case, not presented here, in which particle velocities were modified to include inertia and gravitational settling showed negligible variation as compared to the tracer cases.

The model of microphysical growth is described in detail by Shirgaonkar and Lele (2007). In summary, each ice particle is treated as a spherical nucleus over which ice has deposited. Particle radius changes due to deposition or sublimation of water to or from the particle surface. The growth rate of a single ice particle is calculated using a simple diffusion model (Kärcher et al., 1996). Growth rates are calculated for each computational particle based on the water vapor density field interpolated to the particle location and integrated over the time step. The source term, ω_Y, is then calculated by integrating the source of water vapor within each Eulerian control volume. The water vapor source term is also coupled to the temperature equation through latent heat release, calculated with Eq. 7.

$$\rho_0 C_p \omega_T = -\omega_Y L \tag{7}$$

2.2 Simulation Description

For each of the cases presented here, ambient conditions are as follows: the potential temperature gradient is stable with $d\theta_y/dy = 2.5\,\mathrm{K/km}$, the water vapor gradient approximates a constant ambient relative humidity with respect to ice (RHi), and reference air density, temperature, and pressure are consistent with a cruise altitude of 10.5 km in a standard atmosphere.

For each simulation, a background field of periodic, decaying turbulence is scaled such that its energy matches the inertial subrange spectra for the given case turbulent dissipation rate, ϵ, as given in Table 1. A two-dimensional aircraft wake velocity field is then added to the background field, extruded in the flight direction. The initial flow field consists of two counter-rotating, descending vortices created by the lifting wing of the aircraft and two jet plumes corresponding to the jet engine exhaust. The jet plumes have temperature and humidity profiles consistent with typical cruise operating conditions. Ice particle nuclei are also introduced in the jet plumes with number density proportional to the jet exhaust concentration and

corresponding to an emission index of 10^{15} #/kg fuel.

A series of six unstructured, periodic grids is used to simulate the development of the contrail, with grid resolution maximized in the contrail structure and decreased out to the domain boundaries. Results on each grid are interpolated to the next, with resolution, area of grid refinement, and total domain size adjusted to balance resolution of flow structures, reasonable computational cost, and accurate results. Maximum resolution ranges from $b/128$ to $b/16$ from early to late stages of the simulation, with b the geometric span of the aircraft wake simulated. Similarly, total domain width and height range from $8b$ to $32b$ as the simulation progresses, with the streamwise (z-direction) length remaining constant at $8b$. Grid sensitivity studies show little variation in results due to these transitions from one grid to the next. A total of 8×10^6 computational particles are tracked in each simulation.

Case		ϵ (m^2/s^3)	Vertical Shear (s^{-1})	RHi (%)
A	Moderate turbulence	0.0001	0	130
B	High turbulence	0.001	0	130
C	Moderate shear	0.0001	0.005	130
D	High shear	0.001	0.01	130
E	Medium 2-engine	0.0001	0	130
F	Large 4-engine	0.0001	0	130
G	Small 2-engine	0.0001	0	130
H	Large 4-engine	0.0001	0.005	130
L	Moderate supersaturation	0.0001	0	120
M	Low supersaturation	0.0001	0	110

Table 1: Summary of simulation case parameters.

The results from ten cases are presented here, as summarized in Table 1. The first set of four cases vary ambient turbulence and vertical shear. These cases use an initial condition wake field based on a RANS simulation of a Boeing 767. For cases C and D, the periodic boundary conditions were modified in the vertical direction to simulate vertical wind shear. The second set of four cases vary the aircraft type and number of engines. These cases use an idealized initial condition wake field with counter-rotating Lamb-Oseen vortices and Gaussian exhaust jets. For case H, the periodic boundary conditions were again modified to allow vertical wind shear. The final two cases vary the ambient relative humidity with respect to ice and use the same initial condition wake field as case E.

Table 2 shows the parameters used to define the initial conditions for the cases. The idealized medium 2-engine initial condition field is based on the RANS field used in cases A-D. The parameters for the other idealized cases are based on estimates of typical operating conditions for aircraft of this size. The jet and vortex core locations are defined relative to the aircraft centerline, which is located at $(x, y) = (0, 2.0)$ spans

in order to allow for vortex descent in the domain. The jets are centered at $(\pm\Delta x_j, 2.0 - \Delta y_j)$ and the vortices at $(\pm\Delta x_v, 2.0)$.

3 Results

Each of the cases listed above has been run for twenty minutes of simulation time. This section first presents the results from a baseline case (case E), then comparisons between the various cases showing sensitivity to parameters.

3.1 Baseline Results

Figure 1 shows a sequence of three-dimensional isosurfaces as the vortex-wake system develops over the first several minutes of the simulation. The counter-rotating vortices are mostly parallel after one minute, but small perturbations grow as ambient turbulence triggers the Crow instability. As the vortices loop off, they push the contrail out quickly in the spanwise direction, developing a characteristic periodic puffy structure. By $t = 300\,\mathrm{s}$, the vortex system has become disorganized, and additional spreading of the contrail occurs as the vortices disperse.

The effect of the vortex wake dynamics on the contrail can be visualized by examining flight-direction averaged contours, which give a cross-sectional view. Figure 2 shows contours of relative humidity and ice mass density in the contrail at early times. At $t = 30\,\mathrm{s}$, the contrail is tightly bound in the descending vortex pair. The interior of the vortex system is near saturation ($RHi = 100\%$) and the ice mass of the contrail is concentrated in the same region. As the vortices descend, the region near saturation extends from the primary wake up into the secondary wake. Since the vortices have linked by $t = 120\,\mathrm{s}$, the flight-direction is inhomogeneous in the primary wake region, so this region appears to be more supersaturated and contain less ice in the averaged view. By $t = 300\,\mathrm{s}$, the vortices have dissipated, and the primary wake has spread inhomogeneously in the spanwise direction. The region near saturation still extends up into the secondary wake, and ice mass density is greatest in the same central, vertical curtain.

Figure 3 shows contours of relative humidity and ice mass density at later times, corresponding to the dispersion phase of the simulation. In this phase, the development of the contrail is dominated by turbulent mixing of the aircraft exhaust plume with ambient air. The motion of the vortex system is no longer organized, but the energy remaining in the primary wake spreads the contrail horizontally. Vertical motions of the contrail are driven by buoyancy effects. As the energy of the aircraft wake dissipates, atmospheric

		Medium 2-Engine	Large 4-Engine	Small 2-Engine	
b	Wing span	47.2	64.5	34.3	m
V_0	Cruise speed	236.9	236.9	233.4	m/s
Γ_0	Initial Circulation	391	646	246	m^2/s
n/L_z	Ice concentration	5.79×10^{12}	1.16×10^{13}	2.50×10^{12}	#/m
r_j	Jet core radius	0.15	0.11	0.15	spans
Δx_j	Jet core location	0.26	$0.18, 0.32$	0.14	spans
Δy_j	Jet core location	0.16	0.16	0.16	spans
r_v	Vortex core radius	0.07	0.07	0.07	spans
Δx_v	Vortex core location	0.41	0.39	0.39	spans

Table 2: Simulation parameters for the idealized initial condition fields.

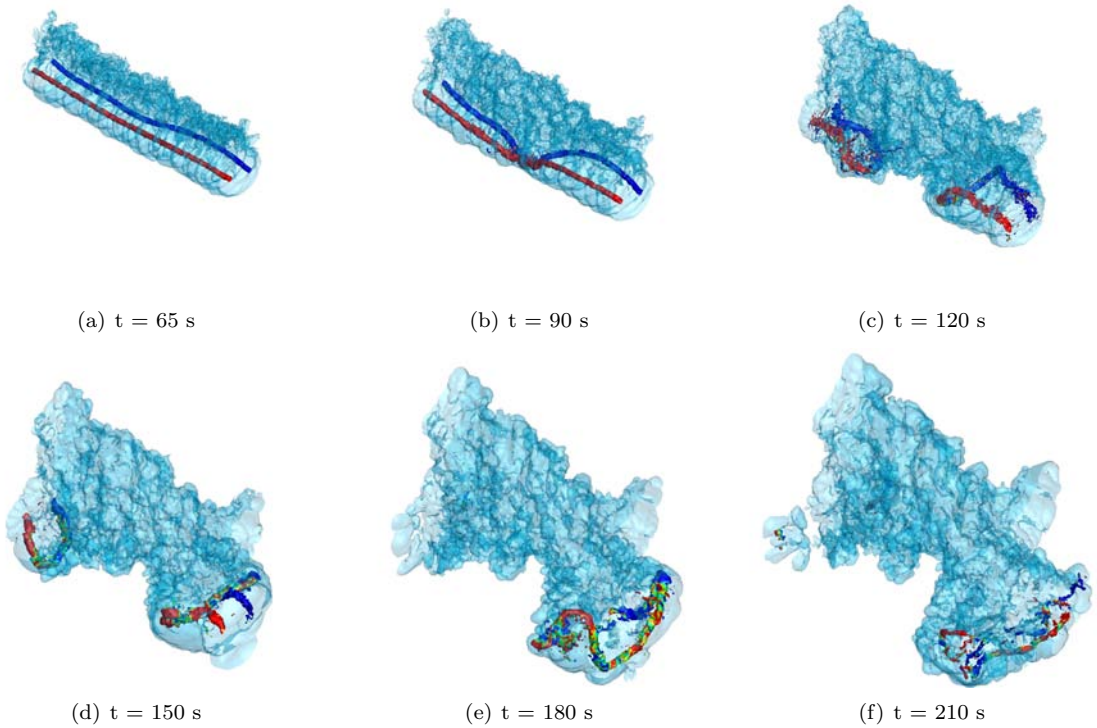

(a) t = 65 s (b) t = 90 s (c) t = 120 s

(d) t = 150 s (e) t = 180 s (f) t = 210 s

Figure 1: Time sequence of the vortex wake breakdown and contrail, from 60 to 210 seconds after emission, for case E. The opaque isosurfaces show vorticity magnitude, colored by streamwise vorticity. The transparent isosurface shows the outer extent of a passive exhaust scalar.

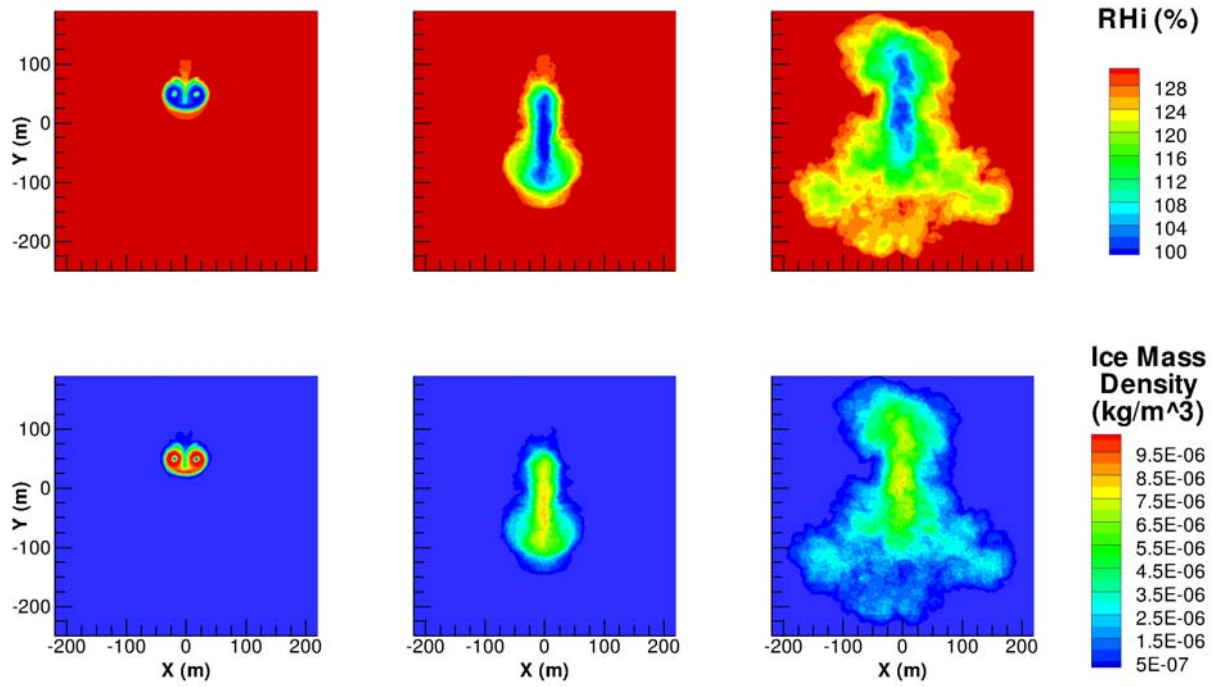

(a) t = 30 s (b) t = 120 s (c) t = 300 s

Figure 2: Flight-direction averaged contours of relative humidity with respect to ice (top) and ice mass density (bottom) at three early times for case E.

turbulence comes to dominate the mixing of humid ambient air into the contrail. As the contrail spreads from $t = 600\,\mathrm{s}$ to $1200\,\mathrm{s}$, the entrainment of ambient water vapor into the contrail is seen in the increase of ice mass density in the central region. The region of near saturation humidity also grows in the averaged view as mixing re-homogenizes the contrail in the flight direction.

The general behavior of ice growth in the contrail is the same for all of the cases, and can be seen in the domain-integrated ice size distributions shown in Fig. 4. From the initial monodisperse particle size, ice grows very quickly at the beginning of the simulation to a narrow distribution of sizes as the water vapor emitted in the jet exhaust deposits on the particles (Fig. 4(a)). During the remainder of the vortex phase, humid ambient air is entrained and some larger particles grow, while some smaller particles in the interior of the contrail sublimate due to locally subsaturated conditions. The result is a broadening of the size distribution (Fig. 4(b)). As the vortices dissipate and the contrail enters the dispersion phase, the entrainment of humid air by mixing dominates ice growth, and the distribution moves toward larger particle sizes (Fig. 4(c)).

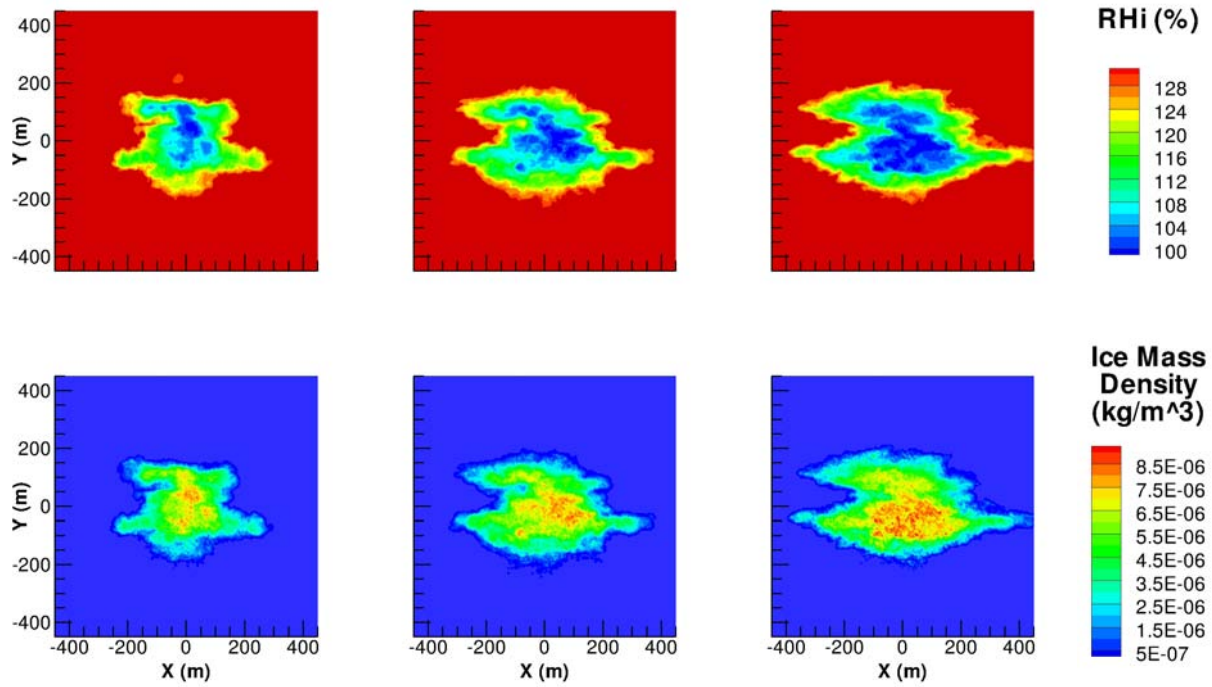

(a) t = 600 s (b) t = 900 s (c) t = 1200 s

Figure 3: Flight-direction averaged contours of relative humidity with respect to ice (top) and ice mass density (bottom) at three late times for case E.

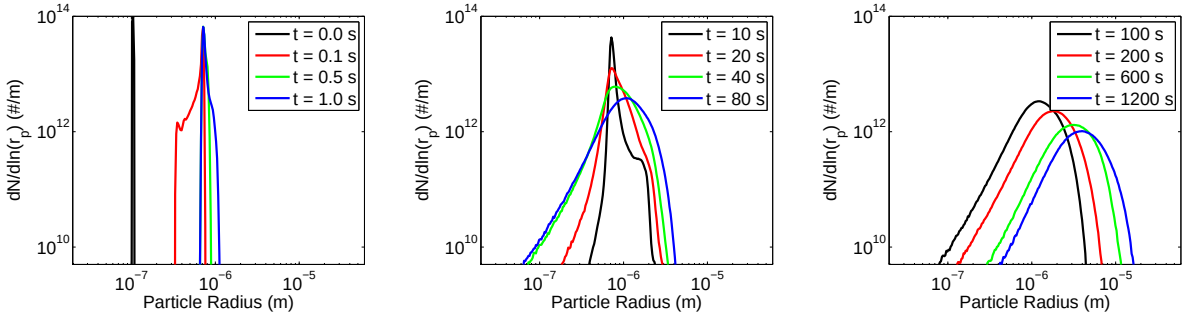

(a) Early times. (b) Vortex phase. (c) Dispersion phase.

Figure 4: Domain-integrated ice particle size PDFs for case E at a series of times throughout the simulation.

3.2 Case Comparisons

As noted in the introduction, much of the uncertainty in estimating the climate effects of contrails and induced cloudiness results from a lack of observational data of global contrail coverage and optical properties. This analysis will therefore focus on the contrail features relevant to these properties, namely the nature of the ice content of the contrails and their geometric extent. Optical depth characterizes the radiative transfer through the contrail at a particular wavelength, while cross-sectional width characterizes the area covered by the contrail assuming some uniform conditions along the flight path. These quantities are used here as convenient properties for comparing between cases.

Contrail optical depth and width are derived from the simulation data by post-processing as shown schematically in Fig. 5. First, contrail optical extinction, τ, is calculated for each 3D grid cell in the domain,

$$\tau = \sum_{i=1}^{N} \pi r_i^2 Q_i \frac{N_p}{\Delta V}, \tag{8}$$

where N is the number of computational particles in the grid cell, r is particle radius, ΔV is the volume of the grid cell, and Q is the scattering efficiency calculated as a function of particle radius using Lorenz-Mie theory. These values are averaged in the flight direction, then integrated in the vertical direction to produce an optical depth across the width of the contrail. A Gaussian curve is fit to this distribution. Figure 6 shows optical depth and projected width plotted against simulation time for each of the parameter categories. These quantities are only available at discrete times when the relevant data were saved. As shown in Fig. 5, the optical depth reported in Fig. 6 is the amplitude of the fit Gaussian, while the contrail width reported is 4σ, where σ^2 is the variance of the fit Gaussian.

The behavior of contrail optical depth and width is similar for each case and is worth discussing before sensitivities are addressed. In each case, the optical depth increases through the vortex phase, reaches a maximum, and then decreases through the dispersion phase. Correspondingly, the width decreases slightly through the vortex phase, reaches a minimum, and then increases through the dispersion phase. As shown in the previous section, during the vortex phase the contrail is tightly bound to the vortices. Ice growth occurs within a relatively constant width region, increasing the ice number density, average radius, and thus optical depth there. As the contrail enters the dispersion phase, this horizontal confinement ends and the spanwise spreading of the contrail decreases its optical depth while increasing its width. Although width continues to increase throughout the simulation, the entrainment of humid ambient air and subsequent ice growth balances the dilution of the contrail, and optical depth appears to reach an asymptotic value by the

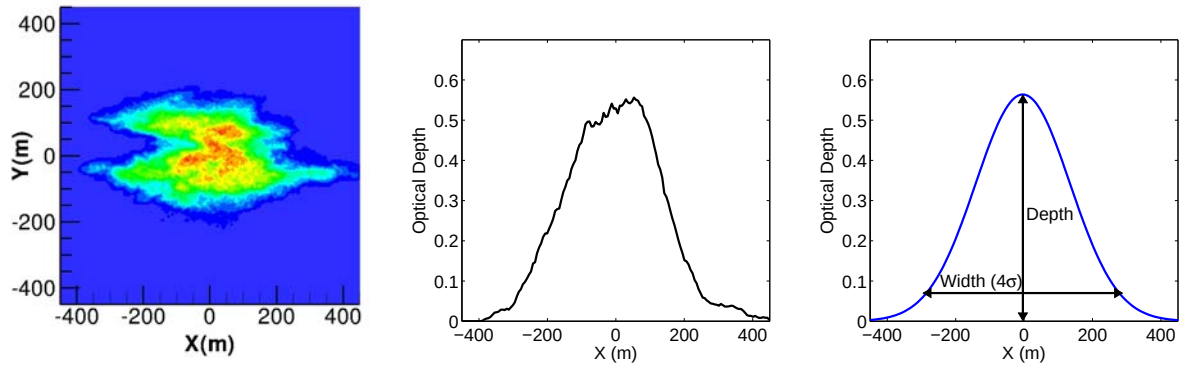

(a) Z-averaged optical extinction. (b) Optical depth. (c) Gaussian fit.

Figure 5: Sequence of the process used to calculate optical depth and contrail width. Ice data from the LES is first used to calculate optical extinction throughout the 3D domain. Optical extinction is then averaged in the flight (z) direction (a) and integrated in the vertical (y) direction to calculate optical depth across the contrail (b). A Gaussian fits the resulting curve well, especially at late times (c). The data plotted here are for case E at 1200 seconds.

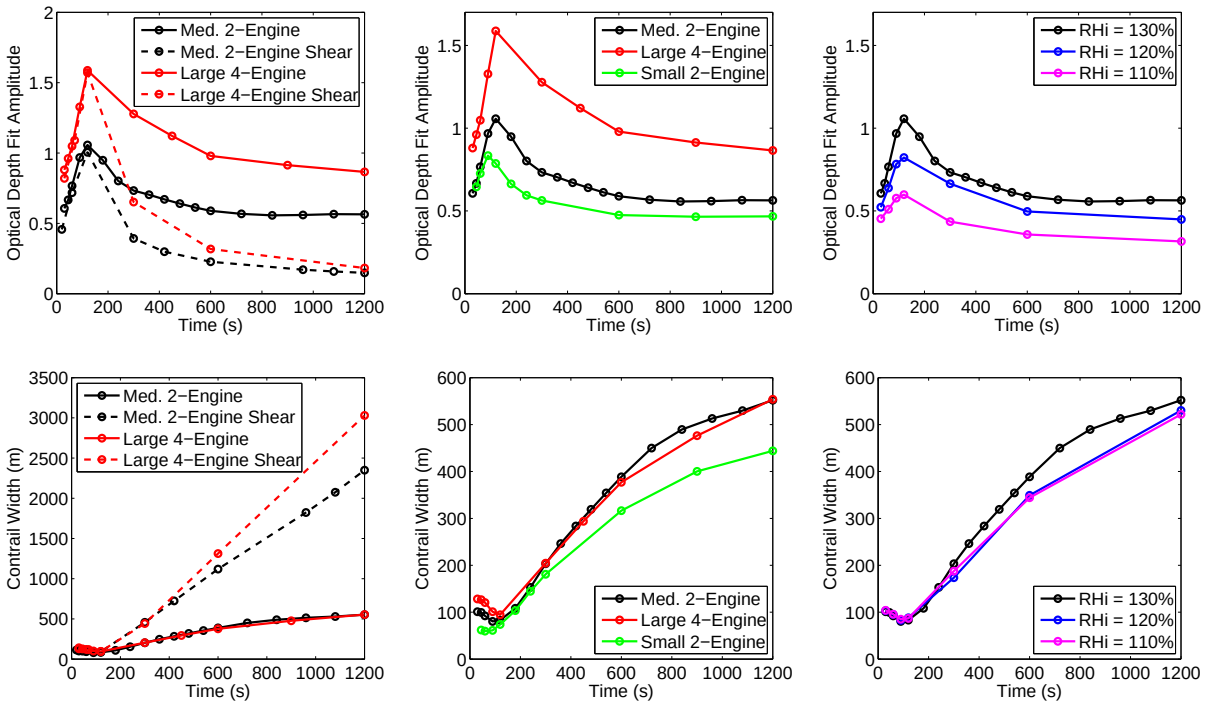

(a) Vertical wind shear cases. (b) Aircraft type cases. (c) Ambient humidity cases.

Figure 6: Domain-integrated optical properties for the sensitivity cases showing optical depth amplitude (top) and contrail width (bottom). Line styles are the same for each top and bottom pair of plots. The data in (a) correspond to cases E, C, F and H; the data in (b) correspond to cases E, F, and G; and the data in (c) correspond to cases E, L, and M.

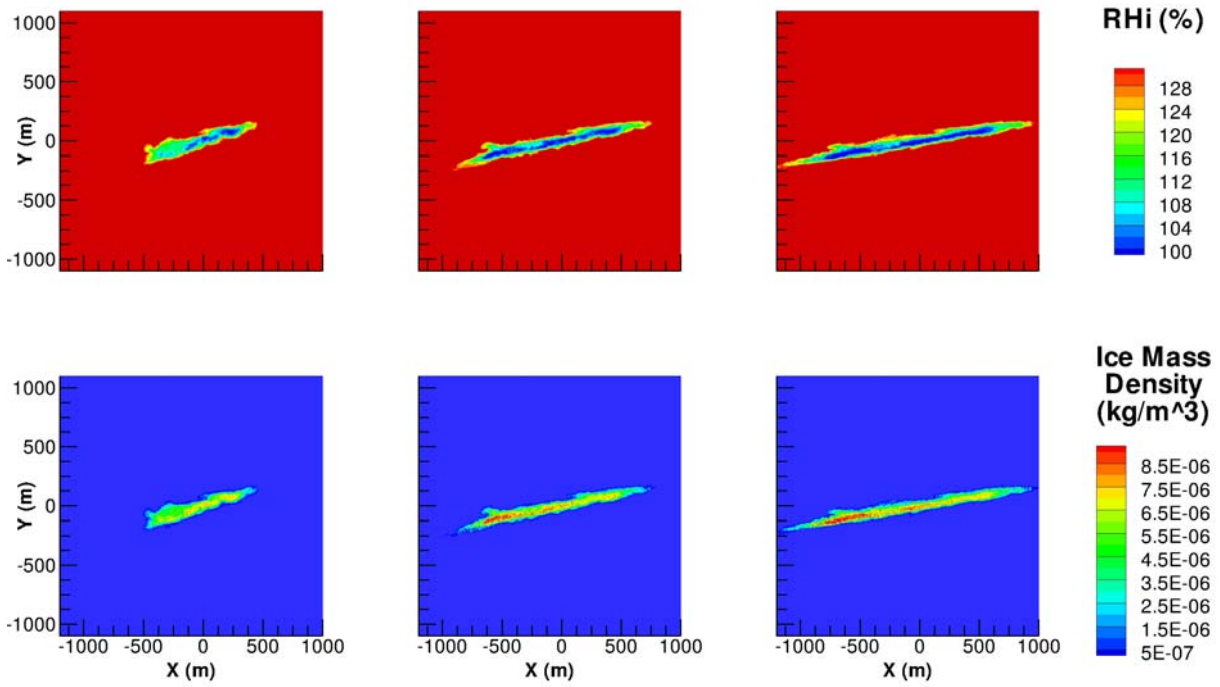

(a) t = 600 s (b) t = 900 s (c) t = 1200 s

Figure 7: Flight-direction averaged contours of relative humidity with respect to ice (top) and ice mass density (bottom) at three late times for case C.

end of the simulation.

Trends for each of the parameter categories are evident in these results. For the wind shear cases, the kinematic effect of shear in spreading the contrail horizontally dominates both the optical depth and the width in the dispersion phase. As the contrail is sheared, it becomes geometrically shallower and wider, reducing its optical depth and increasing its width. Figure 7 replicates Fig. 3 for the moderate shear case C, and illustrates this dramatic kinematic effect.

The aircraft type cases show an increase in optical depth for larger aircraft. This reflects competing effects in these cases. Larger aircraft emit more particles due to more fuel being burned. Because larger aircraft have a larger span, their wake is larger in the initial condition, so the volume that these particles are dispersed in is larger. This wider dispersion is evident in the contrail width plot at early times. The greater volume is not large enough, however, to overcome the higher number of particles emitted, so number density and therefore optical depth are larger for larger aircraft. Although this trend in optical depth continues to late times for these cases, the trend in contrail width does not, as the Medium and Large aircraft have

nearly the same width at the end of the simulation. This emphasizes that ambient turbulence dominates late spreading of the contrail, and differences at late stages are largely due to the specific turbulent realizations of individual simulation cases.

The ambient humidity variation cases also show a clear trend in contrail optical depth. In the higher humidity cases, more water vapor is available to deposit onto the contrail ice, leading to larger particles. The increase in particle radius is reflected in increased optical depth with humidity. Contrail width appears to be somewhat reduced by lower humidity at late times, but again the specific turbulent realizations of each case likely cause the small differences shown here.

4 Conclusions

The global simulations that are used to estimate the climate effects of human activities resolve scales much larger than individual contrails. Simple parametric models are thus required to represent contrails when the physics simulated here cannot be resolved. The parameter variations chosen for investigation in this work represent only a small portion of the large parameter space of commercial aircraft flight conditions. Still, the results point toward the parameters on which contrail properties depend most sensitively, and therefore the parameters that should be addressed in models.

For optical depth and contrail width, the strongest sensitivity in the simulations was to vertical wind shear. The quantitative comparisons detailed here are all given for results after twenty minutes of simulation time. For the two cases simulating a large, 4-engine aircraft at 130% RHi, a moderate vertical wind shear of $0.005\,\mathrm{s}^{-1}$ reduced the peak optical depth by 79% as compared to the zero shear case, from 0.87 to 0.18. Shear increased the width by 450% as compared to the zero shear case, from 550 m to 3000 m. Shear caused a similar magnitude reduction of optical depth and increase of width in the medium, 2-engine aircraft cases.

The other major parameter variations presented here, aircraft type and ambient humidity, had little effect on contrail width in the long term, as ambient turbulence dominated the horizontal spread of the contrails. Optical depth was sensitive to both of these parameters. Under the same 130% RHi condition, the large, 4-engine aircraft produced a peak optical depth of 0.87, 53% larger than the medium, 2-engine aircraft peak depth of 0.56. The small, 2-engine aircraft contrail had a peak optical depth of 0.47, 17% lower than the medium aircraft. Finally, the 120% and 110% RHi cases had peak optical depths of 0.45 and 0.32, 20% and 43% lower than the baseline 130% RHi case respectively.

The work reported here is intended to support the development and improvement of a global climate

model that calculates the climate impact of aviation (Jacobson et al., 2010a,b). The climate model uses a parametric sub-grid scale model called the SPM (Naiman et al., 2010) to represent contrail dynamics. The SPM takes grid scale vertical shear and turbulence parameters as inputs and predicts the geometric shape of contrails over time. Comparison of sheared LES results with the SPM under the same conditions show that it accurately predicts contrail width as it grows under shear. The LES results presented here thus serve as validation for the SPM used in climate calculations.

Several additional items of work are planned to improve and extend the simulations presented in this report. The twenty minutes simulated by LES is less than a typical global climate model time step. Proper validation of the SPM will require running the LES for several climate model time steps (two or three hours of simulation time). For these longer time runs, several extensions to the LES will be implemented. A new ice microphysical model will be added to include the effects of sedimentation on ice particle locations, which becomes more important at later times as ice particles continue to grow. More realistic ice crystal shapes will be included through a model of ice habit. Large scale turbulence, which is responsible for spreading contrails as they age, will be forced in the fluid dynamics model. The results of these longer time runs will be used to further improve the modeling of contrails within the global model to reduce uncertainties in the magnitude of aviation climate impacts.

Acknowledgments

This project is sponsored by the Federal Aviation Administration through the Partnership for AiR Transportation Noise and Emissions Reduction (PARTNER), an FAA-NASA-Transport Canada sponsored Center of Excellence, under award number DTFAWA-05-D=0006. Any opinions, findings, and conclusions or recommendations expressed in this material are those of the authors and do not necessarily reflect the views of the FAA, NASA, or Transport Canada. This research is also supported in part by the National Science Foundation through TeraGrid resources provided by LONI and NCSA under grant number TG-CTS080041N. Thanks also to Dr. Frank Ham (Stanford), Dr. Mohan Gupta (FAA), Dr. Anup Shirgaonkar (MIT), and Dr. Steven Baughcum (Boeing).

References

A. Chlond. Large-eddy simulation of contrails. Journal of the Atmospheric Sciences, vol. 55, no. 5, pages 796–819 (1998).

S. C. Crow. Stability theory for a pair of trailing vortices. AIAA Journal, vol. 8, pages 2172–2179 (1970).

F. Ham, K. Mattsson, G. Iaccarino, and P. Moin. *Complex Effects in Large Eddy Simulation*, Springer, chap. Towards Time-Stable and Accurate LES on Unstructured Grids (2007).

M. Z. Jacobson, J. T. Wilkerson, A. D. Naiman, and S. K. Lele. The effects of aircraft on climate and pollution. Part I: A model that treats the subgrid evolution of discrete size- and composition-resolved contrails from all commercial flights worldwide. Journal of Geophysical Research - Atmospheres (2010a). In review.

M. Z. Jacobson, J. T. Wilkerson, A. D. Naiman, and S. K. Lele. The effects of aircraft on climate and pollution. Part II: decadal-scale impacts of exhaust from all commercial aircraft worldwide treated at the subgrid scale. Journal of Geophysical Research - Atmospheres (2010b). In review.

E. J. Jensen, A. S. Ackerman, D. E. Stevens, O. B. Toon, and P. Minnis. Spreading and growth of contrails in a sheared environment. Journal of Geophysical Research, vol. 103, no. D24, pages 31,557–31,567 (1998).

B. Kärcher, T. Peter, U. M. Biermann, and U. Schumann. The initial composition of jet condensation trails. Journal of the Atmospheric Sciences, vol. 53, pages 3066–3083 (1996).

D. S. Lee, D. W. Fahey, P. M. Forster, P. J. Newton, R. C. N. Wit, L. L. Lim, B. Owen, and R. Sausen. Aviation and global climate change in the 21st century. Atmospheric Environment, vol. 43, pages 3520–3537 (2009).

D. C. Lewellen and W. S. Lewellen. The effects of aircraft wake dynamics on contrail development. Journal of the Atmospheric Sciences, vol. 58, no. 4, pages 390–406 (2001).

K. Mahesh, G. Constantinescu, and P. Moin. A numerical method for large-eddy simulation in complex geometries. Journal of Computational Physics, vol. 197, pages 215–240 (2004).

A. D. Naiman, S. K. Lele, J. T. Wilkerson, and M. Z. Jacobson. Parameterization of subgrid plume dilution for use in large-scale atmospheric simulations. Atmospheric Chemistry and Physics, vol. 10, no. 5, pages 2551–2560 (2010).

R. Paoli, J. Helie, and T. Poinsot. Contrail formation in aircraft wakes. Journal of Fluid Mechanics, vol. 502, pages 361–373 (2004).

R. Paoli, F. Laporte, and B. Cuenot. Dynamics and mixing in jet/vortex interactions. Physics of Fluids, vol. 15, no. 7, pages 1843–1860 (2003).

R. Paugam, R. Paoli, and D. Cariolle. Influence of vortex dynamics and atmospheric turbulence on the early evolution of a contrail. Atmospheric Chemistry and Physics, vol. 10, pages 3933–3952 (2010).

U. Schumann. Formation, properties, and climatic effects of contrails. Comptes Rendus Physique, vol. 6, pages 549–565 (2005).

A. A. Shirgaonkar and S. K. Lele. Large eddy simulation of early stage aircraft contrails. Tech. Rep. No. TF-100, Flow Physics and Computational Engineering Group, Department of Mechanical Engineering, Stanford University (2007).

E. A. Spiegel and G. Veronis. On the boussinesq approximation for a compressible fluid. The Astrophysical Journal, vol. 131, pages 442–447 (1960).

S. Unterstrasser and K. Gierens. Numerical simulations of contrail-to-cirrus transition part 1: An extensive parametric study. Atmospheric Chemistry and Physics, vol. 10, no. 4, pages 2017–2036 (2010a).

S. Unterstrasser and K. Gierens. Numerical simulations of contrail-to-cirrus transition part 2: Impact of initial ice crystal number, radiation, stratification, secondary nucleation and layer depth. Atmospheric Chemistry and Physics, vol. 10, no. 4, pages 2037–2051 (2010b).

S. Unterstrasser, K. Gierens, and P. Spichtinger. The evolution of contrail microphysics in the vortex phase. Meteorologische Zeitschrift, vol. 17, no. 2, pages 145–156 (2008).

Student Biography

Alexander is a Ph.D. candidate in the Department of Aeronautics and Astronautics at Stanford University. He is a sixth year student in the Unsteady Flow Physics and Aeroacoustics Laboratory directed by Professor Sanjiva Lele. In addition to his research on the impact of aviation on the environment, he is interested in the design of and flight path planning for unmanned aerial vehicles. He previously earned a B.S.E. in Mechanical and Aerospace Engineering at Princeton University and a M.S. in Aeronautics and Astronautics at Stanford University.